



Laboratory Shear Behavior of Tensile- and Shear-Induced Fractures in Sandstone: Insights from Acoustic Emission

Shuting Miao¹ · Peng-Zhi Pan^{2,3} · Arno Zang¹ · Chuanqing Zhang^{2,3} · Hannes Hofmann^{1,4} · Yinlin Ji¹

Received: 7 August 2023 / Accepted: 16 January 2024 / Published online: 5 March 2024
© The Author(s), under exclusive licence to Springer-Verlag GmbH Austria, part of Springer Nature 2024

Abstract

The distinction between the shear behavior of tensile- and shear-induced fractures is critical to understanding the deformation and failure of geologic discontinuities at different scales. To investigate these differences, a series of direct shear tests were performed on sandstone specimens with a continuous fracture created by either splitting or shearing. The acoustic emission (AE) technique was used to examine variations in grain-size cracking behavior between specimens with tensile- and shear-induced fractures. An increase in normal stress for both fracture types correlates with increased microcrack density and energy release. However, there are notable differences: during the shear process, tensile-induced fractures produce AE sequences similar to the seismic patterns observed along natural tectonic faults, with foreshocks, mainshocks, and aftershocks. In contrast, the AE sequence for shear-induced fractures during the shear process lacks prominent mainshocks and deviates progressively from the power-law function with time as normal stress increases. In addition, the AE b -value for tension-induced fractures initially shows a gradual decrease as the mainshock approaches and then slowly increases during the aftershock period. In contrast, the b -value remains nearly constant for shear-induced fractures due to the low roughness and heterogeneity of the fracture surface. These differences highlight the strong correlation between AE responses and fault heterogeneity, paving the way for fault characterization and risk assessment in subsurface energy extraction.

Highlights

- The cracking behavior of both tensile- and shear-induced fractures in direct shear tests is investigated using the AE technique.
- In direct shear tests, the AE sequences of tensile fractures follow a power law, while a significant deviation from the power law is observed in the AE sequence of shear fractures.
- The power-law evolution of the AE sequence before and after the mainshock, together with anomalous b -values, can be used as indicators to distinguish young faults from mature faults.

✉ Peng-Zhi Pan
pzpan@whrsm.ac.cn

✉ Yinlin Ji
yinlinji@gfz-potsdam.de

¹ Helmholtz Centre Potsdam GFZ German Research Centre for Geosciences, 14473 Potsdam, Germany

² State Key Laboratory of Geomechanics and Geotechnical Engineering, Institute of Rock and Soil Mechanics, Chinese Academy of Sciences, Wuhan 430071, Hubei, China

³ University of Chinese Academy of Sciences, Beijing 100049, China

⁴ Institute for Applied Geosciences, Technische Universität Berlin, 10623 Berlin, Germany

Keywords Direct shear testing · Acoustic emission · Power law · b -value · Fault heterogeneity · Tensile versus shear fractures

1 Introduction

The presence of numerous fractures, joints, and faults in rock masses can lead to unstable shear slip under tectonic stress or human activity, resulting in events such as rock bursts, tunnel collapses, and even anthropogenic/tectonic earthquakes under tectonic stress (Chen et al. 2013; Ji et al. 2022a; Zhang et al. 2022). Understanding the shear behavior and rupture process of these discontinuities is critical not only to capture earthquake nucleation but also to mitigate associated risks and strengthen structural stability in geotechnical or geothermal engineering sites (Badt et al. 2016; Singh and Basu 2016; Niktabar et al. 2017; Luo et al. 2022; Bolton et al. 2023). Due to its inherent complexity, the study of shear behavior within natural discontinuities in the upper crust is challenging, involving high costs and technical implementation difficulties (Bolton et al. 2023; Borate et al. 2023). Consequently, extensive research has focused on understanding the shear behavior of rock fractures, joints, and faults through experimental and numerical studies (Li et al. 2014, 2022; Badt et al. 2016; Meng et al. 2016a; Ji et al. 2022b; Zhang et al. 2022). These studies have demonstrated the importance of normal stress, rock stiffness, fracture roughness, and the presence of gouges in determining shear behavior (Byerlee 1970; Badt et al. 2016; Niktabar et al. 2017).

Shear fractures and faults are widespread in the brittle Earth's crust and are documented by earthquake activity in the compressive stress regime (Kim et al. 2003). In contrast, tensile fractures require specific geological conditions with low confining stresses, such as dike intrusion, volcanic magma rise, and geothermal unrest (Einstein 2021). Replicating these natural joints or faults has long been a concern, primarily due to the laborious and time-consuming processes involved in sampling and transporting natural fractures (Vogler et al. 2017; Zhang et al. 2023). As a result, laboratory-generated fractures are often used as surrogates for in-situ fractures or faults. By applying mechanical loads to rocks with pre-existing natural fractures, synthetic surfaces have been created to mimic natural fractures (Lei 2003; Lei and Ma 2014; Vogler et al. 2017; Jiang et al. 2020). Alternatively, fractures have been artificially created using methods such as splitting for Mode I fractures (Tang and Wong 2015; Badt et al. 2016; Meng et al. 2016b; Morad et al. 2020) or shearing fractured rock specimens for Mode I/II fractures (Myers and Aydin 2004; Dresen et al. 2020; Miao et al. 2024; Zhang et al. 2023). Recent studies, including

those by Morgan et al. (2013), Vogler et al. (2017), and Zhang et al. (2023), have provided insight into the effects of fracture formation process and fracture mode on fracture topography and roughness. Their results show significant differences in fracture topography between natural and artificial fractures, as well as between tensile and shear fractures. Natural tensile fractures often include the full spectrum of shear fractures found in nature, in addition to artificial tensile and shear fractures. Tensile fractures are typically characterized by a clear texture and absence of wear debris, making them valuable for reflecting fresh and unweathered fractures and joints (Johansson 2016). In contrast, shear fractures or tectonic faults may have experienced some degree of shear slip and contain gouge material (Myers and Aydin 2004; Sagy et al. 2007; Davidesko et al. 2014). In terms of fracture formation, tensile fractures generally exhibit higher roughness than shear fractures, primarily due to their formation under low or suppressed confinement. Conversely, shear fractures are formed by confined shear, which typically results in flatter fractures with lower roughness (Einstein 2021). The differences in fracture characteristics between tensile and shear fractures can lead to different shear responses and cracking behavior during the shear process, an aspect that has not been extensively studied.

The AE technique is widely recognized as an invaluable and versatile tool for the quantitative monitoring of dynamic processes in stressed structures. Parameters such as AE hit (event) rate, amplitude, and energy release rate provide essential insights into the cracking process and precursory signals associated with potential failures (Zang et al. 2000; Triantis and Kourkoulis 2018; Zhang and Zhou 2020; Bolton et al. 2021, 2023; Marty et al. 2023). In addition, some studies have performed detailed statistical analyses of AE sequences from rock cracking (Davidsen et al. 2007). Interestingly, AE events resulting from the rupture of single asperities can exhibit characteristics similar to sequences observed in natural earthquakes, including foreshocks, mainshocks, and aftershock events (Lei 2003; Goebel et al. 2023). These studies have shown that similar to those observed in seismic data, AE sequences from loaded rock specimens can obey empirical scaling laws, such as the Gutenberg–Richter frequency–magnitude scaling (Lei 2003; Goebel et al. 2013b) and the Omori's law for aftershock decay (Lei 2003; Triantis and Kourkoulis 2018; Marty et al. 2023). These studies provide fundamental insights for interpreting AE data and understanding the processes and mechanisms involved in fault rupture. However, few studies have specifically focused on the similarities and differences

in AE responses during the shear process between tensile- and shear-induced fractures.

The purpose of this experimental study is to provide a comparative analysis of the shear behavior between tensile and shear-induced fracture under different normal stresses. Note that shear-induced fracture specifically refers to a fracture induced by compression-shear stress. The type of fracture induced by compression-shear stress can be mixed tensile-shear cracks or shear cracks, and the exact fracture mechanism and topography depend on the applied normal stress. Therefore, different normal stresses are considered to generate the shear-induced fractures to obtain a comprehensive comparison with the tensile-induced fractures. The AE technique is used in this study to provide valuable insight into the cracking behavior within rocks during the shear process. The differences in AE responses between tensile- and shear-induced fractures provide a potential method for

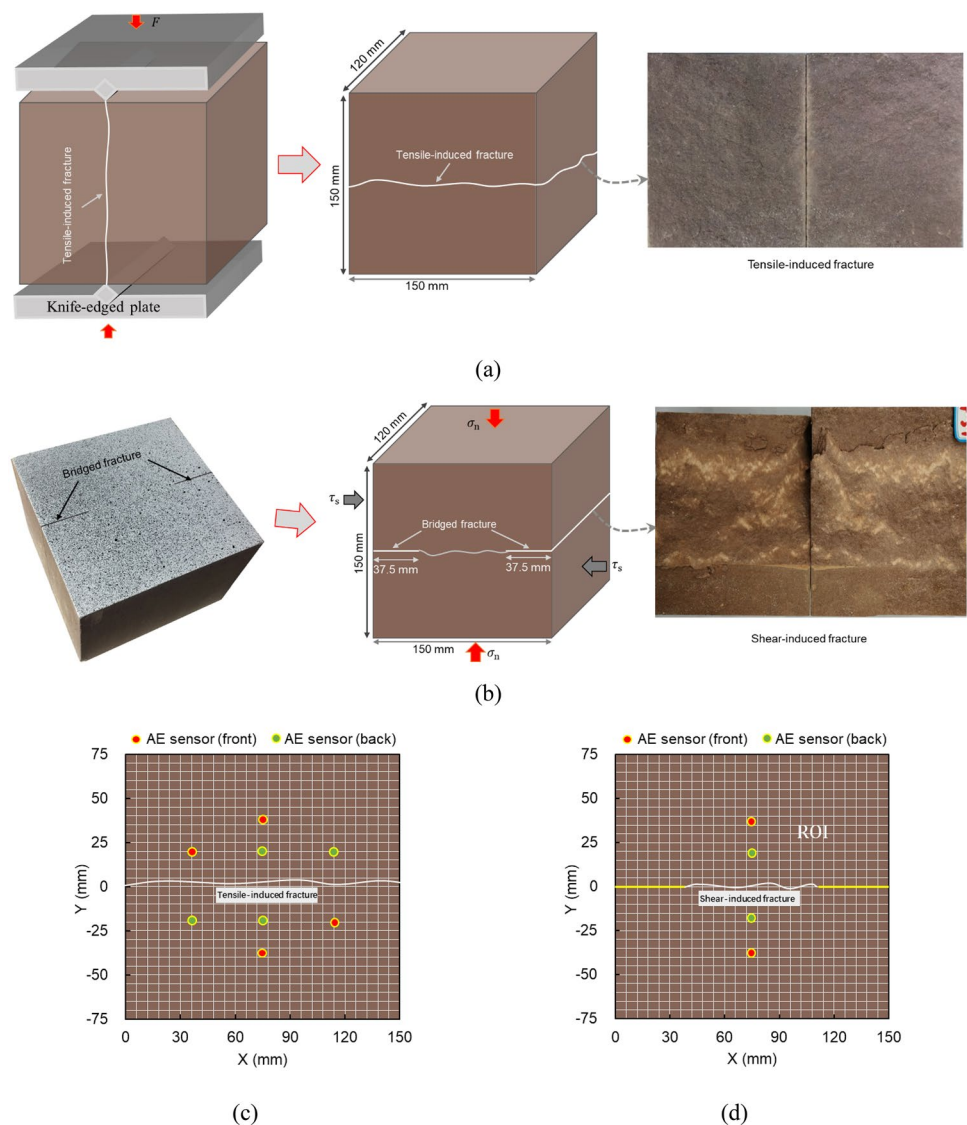
identifying fault characteristics, especially in the absence of effective methods for characterizing fault heterogeneity in laboratory and field.

2 Specimen Preparation and Testing

Homogeneous red sandstone with a uniaxial compressive strength of 58 MPa and Young's modulus of 9.87 GPa was used in this study. Rectangular prism specimens measuring 150 mm (width) × 150 mm (height) × 120 mm (thickness) were carefully cut from a large block and polished to ensure flatness and perpendicularity.

The tensile-induced fracture was created using a special mold, similar to that used in the Brazilian disk splitting test, as shown in Fig. 1a. This mold consists of two prismatic alloy bars as stress concentrators and two square iron plates with

Fig. 1 **a** Dimensions and formation process of sandstone specimens with a tensile-induced fracture. The right subfigure displays an example of a tensile-induced fracture. **b** Dimensions of sandstone specimens with bridged fractures and formation process of shear-induced fracture. The shear-induced fracture in this study specifically refers to compression-shear-induced fracture. The right subfigure displays an example of a shear-induced fracture with a shear trace and gouge, formed under $\sigma_n = 5$ MPa. **c, d** Placement of AE sensors on specimens with tensile- and shear-induced fractures, respectively. The red and green points denote sensors on the front and back sides, respectively



a trough in the center. For more detailed information on the mold, see Meng et al. (2016b). To facilitate the positioning of the prismatic alloy bars, a predetermined cleavage path was marked in the center of the specimens. The axial force was then gradually applied to the top plate, resulting in the formation of a rough surface characterized by interlocking asperities. The splitting process (Fig. 1a left), an illustration of a tensile-induced fracture trace (Fig. 1a middle), and the corresponding fracture surface (Fig. 1a right) are shown in Fig. 1a.

To generate shear-induced fractures, direct shear tests were performed on bridged fracture specimens (Fig. 1b, left). These specimens were prepared by cutting two straight fractures, each 37.5 mm long and 1.5 mm wide, on the left and right sides of intact rectangular prism specimens. Shearing of the rock bridge eventually results in the formation of a continuous fracture, called a shear-induced fracture (Fig. 1b center). The right subfigure of Fig. 1b shows an example of a shear-induced fracture formed at $\sigma_n = 5$ MPa. The presence of gouges and scratches on the fracture surface reveals the shear history during the formation of the shear-induced fractures. Note that the shear area for the tensile-induced fracture is more than twice that of the shear-induced fracture. This is because the pre-existing fractures with an opening of 1.5 mm do not make their surfaces contact during the entire shear process.

The direct shear tests were performed on a servo-controlled direct shear apparatus at a constant shear displacement rate of 0.5 mm/min under an imposed constant normal stress. Different normal stress loading schemes were considered in this study and are listed in Table 1. The shear tests on tensile- and shear-induced fractures were conducted under the same normal stress conditions of 3 MPa, 5 MPa, and 8 MPa. However, the minimum normal stress was set at 1 MPa for tensile-induced fractures and 0.5 MPa for shear-induced fractures. Since our primary focus is on the temporal distribution of AE activities, the slight difference in the minimum normal stress does not affect our conclusion. It is important to note that the test was not stopped after the generation of shear-induced fractures, except for one specimen that was unloaded after shearing the rock bridge to examine the shear-induced fracture surface (as shown in Fig. 1b, right). Instead, shear displacement was continuously applied to the shear-induced fracture at the same displacement rate. Using this continuous loading style, we avoid changing the relative position of the upper and lower blocks. The tests were terminated after reaching a stable

post-peak residual state. The displacements in both the normal and shear directions were calibrated using the stiffness of the loading system. During the tests, loads and displacements were recorded by the data acquisition system at intervals of 0.2 s. The calculation of normal and shear stresses is based on the actual contact area, following the methodology documented by Meng et al. (2022). For further details on the design, construction, and operation of this device, please refer to the works of Zhang et al. (2019) and Cui et al. (2022). To ensure reliable results, three specimens were tested for each loading scheme and configuration.

The AE technique was applied to all rock specimens to monitor the micro-fracturing process during the direct shear tests. Four to eight AE sensors were attached to the front and back surfaces of the rock specimens using Vaseline coupling and adhesive tape. The configuration of the AE sensors is shown in Fig. 1c, d. For continuous recording of the AE waveforms, a 16-channel signal monitoring system (PCI-2) was used at a sampling rate of 2 MHz, with the gain and trigger threshold set to 40 dB.

3 Methodology for Data Processing

3.1 Quantification of Accelerating Failure Processes

3.1.1 A Brief Overview of the Method

Accelerating failure processes are critical phenomena observed in various natural hazards such as landslides, volcanic eruptions, and earthquakes (Voight 1988; Hardebeck et al. 2008). An example of such behavior is the accelerating creep observed in laboratory experiments, which serves as a representative illustration of self-sustaining accelerating failure. To quantitatively characterize the accelerating dynamics before failure, Voight (1988) introduced an empirical equation:

$$\dot{\Omega}^{-\alpha} \ddot{\Omega} = A. \quad (1)$$

Here, Ω represents the response quantity, such as deformation, strain, or cumulative energy release. The dots denote the first and second derivatives of Ω to time. The parameter

Table 1 Normal stress σ_n and its ratio to uniaxial compressive strength σ_n/σ_c for specimens with a tensile- and shear-induced fracture

| Type of fracture | σ_n (MPa) | σ_n/σ_c | σ_n (MPa) | σ_n/σ_c | σ_n (MPa) | σ_n/σ_c | σ_n (MPa) | σ_n/σ_c |
|--------------------------|------------------|---------------------|------------------|---------------------|------------------|---------------------|------------------|---------------------|
| Tensile-induced fracture | 1 | 0.0172 | 3 | 0.0517 | 5 | 0.0862 | 8 | 0.1379 |
| Shear-induced fracture | 0.5 | 0.0086 | 3 | | 5 | | 8 | |

α quantifies the degree of nonlinearity in the process, while A is a constant.

For a specific response quantity, Eq. (1) can be further expressed as follows (Voight 1988):

$$\dot{\Omega} = K(1 - t/t_F)^{\beta_F}, \quad (2)$$

where t represents the time as the controlling variable, t_F denotes the failure time, and K is defined as $K = [A(\alpha - 1)]^{1/(1-\alpha)}$. Additionally, the parameter β_F is calculated as $\beta_F = -1/(1 - \alpha)$. At the rupture point, an infinitesimal increase in the control variable results in a finite increase in the response quantities, causing $\dot{\Omega}$ to diverge and exhibit a singularity (Voight 1988; Hao et al. 2013). This power-law function provides a tool for the analysis of accelerating failure processes, which contributes to the understanding and prediction of catastrophic events in geophysical and geological contexts.

3.1.2 Advanced Data Processing Method

In this study, AE counts serve as the response variable, with recorded time as the controlling parameter. However, capturing the power-law divergence at the rupture point as the failure approaches becomes challenging, especially with a large time window. To address this, an alternative approach proposed by Triantis and Kourkoulis (2018) used a fixed event window to assess the change in the response quantity to the variation in the controlling variable. Determining the response quantity for AE sequences requires comprehensive seismic catalogs, which contain events that are beyond the scope of completeness (Ouillon and Sornette 2005). Therefore, we consider all events in the target catalog with a magnitude that falls within the linear part of the magnitude–frequency distribution.

Specifically, a sliding window of N consecutive events is defined for calculating the response rate $\dot{\Omega}$,

$$\dot{\Omega}(\tau) = \frac{\sum_1^N C_i}{(t_N - t_1)}, \quad (3)$$

where C_i represents the AE counts of the i th event in a given window ($1 \leq i \leq N$), and t_i is the occurrence time of the i th event. τ is the average time paired with $\dot{\Omega}$ and can be calculated as $\tau = \frac{1}{N} \sum_1^N t_i$. In the actual data processing, a window size of 100 events is adopted, and the event window is shifted forward from the starting point at intervals of 25 events or data to mitigate intensive data processing.

3.2 Gutenberg–Richter Law

The Gutenberg–Richter law provides a statistical description of earthquake occurrence and magnitude distribution within

a defined region and over a defined time interval (Gutenberg and Richter 1944). In this study, the Gutenberg–Richter b -value is calculated using the widely used maximum likelihood approach, which accounts for measurement errors and magnitude binning. The b -value estimation equation is written as (Vulcanologia et al. 2003),

$$b = \frac{1}{\ln(10)\Delta M} \ln(q) \quad (4)$$

with

$$q = 1 + \frac{\Delta M}{\hat{\mu} - M_c}, \quad (5)$$

where ΔM represents the bin size, and $\hat{\mu}$ denotes the mean magnitude for the AE sequence. M_c represents the minimum magnitude for the completeness of the AE sequence, independently determined by a bootstrap-based change point detection method (Amorèse 2007). The corresponding asymptotic error is written as (Vulcanologia et al. 2003),

$$\hat{\sigma}_b = \frac{1 - q}{\ln(10)\Delta M \sqrt{nq}}, \quad (6)$$

where n is the total number of events for the b -value calculation. To estimate the b -value, a sliding window of 200 events (i.e., $n = 200$) is defined to contain enough events for statistical analysis and is advanced along the time series at intervals of 50 events. The bin size is set to 0.05. This approach allows the b -value to be calculated at different segments of the data, providing insight into the temporal variation of magnitudes within the specified time interval.

4 Experimental Results

4.1 Mechanical Behavior of Fractured Specimens

4.1.1 Specimens with a Tensile-Induced Fracture

Figure 2 shows the evolution of shear stress, normal displacement, and dilation coefficient $R = d\delta_n/d\delta_s$ for sandstone specimens with a tensile fracture under different normal stresses. The shear stress of specimens with a tensile-induced fracture is characterized by a linear increase before the first stress drop or strain hardening (Fig. 2). When $\sigma_n = 1$ MPa, several stress drops are observed after the peak shear strength (Fig. 2a). These stress drops coincide with the stepwise increase in normal displacement and the occurrence of extremely high peaks in the dilation coefficient R , called dilation events. The frequent occurrence of dilation events at low normal stress is likely related to the shearing of second-order asperities (Yang et al. 2001). In Fig. 2b, a significant stress drop is observed at the peak shear strength

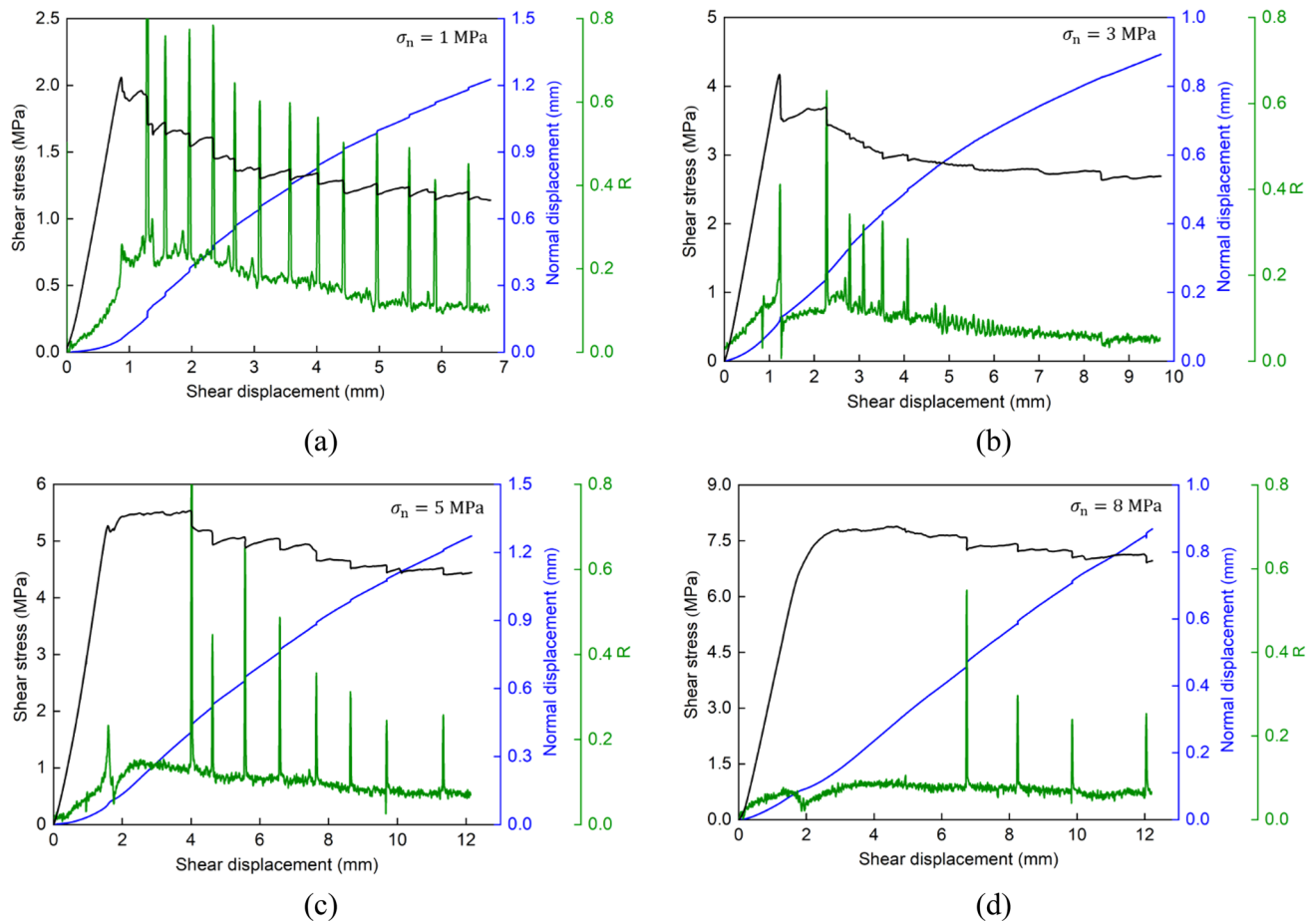


Fig. 2 Evolution of shear stress, normal displacement (δ_n), and dilation coefficient $R = d\delta_n/d\delta_s$ with shear displacement (δ_s) for specimens with a tensile-induced fracture under different normal stresses: **a** $\sigma_n = 1$ MPa, **b** $\sigma_n = 3$ MPa, **c** $\sigma_n = 5$ MPa, and **d** $\sigma_n = 8$ MPa. The

dilation coefficient is calculated based on the slope of normal displacements and shear displacements within a sliding window that encompasses 50 data points

when $\sigma_n = 3$ MPa, which is attributed to the fracture of a few steeply inclined asperities along the tensile-induced fracture. Subsequently, five normal dilation events occur consecutively until the shear displacement reaches 4 mm, after which the dilation coefficient R shows a relatively stable decrease. When $\sigma_n = 5$ MPa, a precursory slip event, characterized by a stress drop of approximately 0.05 MPa, is registered before the peak stress is reached (Fig. 2c). As indicated by Badt et al. (2016), the precursory slip event dissipates some of the stored elastic energy before the subsequent plastic yield. In the subsequent shear weakening phase, a closely distributed stress decrease and eight significant dilation events are observed due to the fracture of the asperities. In Fig. 2d, the rough surface exhibits shear strengthening near the peak shear stress due to elastic deformation and yielding of the asperities on the fracture surfaces (Grasselli 2006). The interlocking or engagement of these asperities under high normal stress (e.g., $\sigma_n = 5$ MPa and 8 MPa) provide additional resistance to the rock material,

often resulting in shear-strengthening behavior. When the shear displacement exceeds 6.5 mm, a further increase in shear displacement triggers the localization and fracture of the asperities, resulting in the occurrence of a dilation event. Throughout the shear process, four notable stress drops accompanied by dilation events are observed until the shear displacement reaches 12 mm.

As shown in Fig. 2, a comparison of the dilation coefficient R reveals distinct dilation and overriding characteristics under varying normal stress conditions. At low normal stresses, the tensile-induced fractures begin to exhibit frequent dilation events at the shear displacement of 1–2 mm (see Fig. 2a). This observation suggests that under low normal stress conditions, the tensile-induced fractures favor normal dilation and overriding at second-order asperities shortly after unstable slip along the fractures. In Fig. 2b, dilation events cease when the shear displacement reaches 4 mm, and the dilation coefficient R begins to exhibit a linear decrease with increasing shear displacement. This behavior

can be attributed to the unique asperity distribution on the tensile fracture surface. At elevated normal stress levels ($\sigma_n=5$ MPa and 8 MPa), the initial dilation event occurs at shear displacements of 4 mm and 6.75 mm, respectively (as shown in Fig. 2c, d). In addition, the displacement interval between adjacent dilation events increases with increasing normal stress. This observation suggests that at higher normal stresses, overriding is predominantly influenced by first-order asperities, which is consistent with the results by Yang et al. (2001) and Grasselli (2006).

4.1.2 Specimens with a Shear-Induced Fracture

Figure 3a illustrates the shearing of the rock bridge leading to the shear-induced fracture, followed by the subsequent shearing behavior of the shear-induced fracture under $\sigma_n = 0.5$ MPa. The loading process is divided into two stages: the shearing of the rock bridge (stage I) and the shearing of the shear-induced fracture (stage II). The shear stress shows a linear increase with increasing shear displacement in stage I, and a significant shear stress drop occurs after the peak stress when the rock bridge is sheared. Figure 3b provides a detailed observation of stage II, which involves shear sliding along the shear-induced fracture. The shear stress initially shows a linear increase, followed by a deviation from this line as it approaches the peak stress. Similar to the observation in Fig. 2a, several stress drops are observed after the peak shear strength of the shear-induced fracture, with six significant dilation events occurring before the termination of the test.

Figure 3c–e illustrates the shearing process of the shear-induced fractures under $\sigma_n = 3$ MPa, 5 MPa, and 8 MPa, respectively. Note that we focus on the shear behavior of the shear-induced fractures and thus the shear of rock bridges before the shear-induced fracture forms is not included. Compared to $\sigma_n = 0.5$ MPa in Fig. 3b, the number of stress drops and dilation events for a given shear displacement decreases significantly under $\sigma_n = 3$ MPa (Fig. 3c). When $\sigma_n = 5$ MPa and 8 MPa, the dilation coefficient gradually decreases and finally stabilizes at an approximately low constant value below 0.07 (Fig. 3d, e). If the dilation events are not taken into account, the average dilation coefficient is significantly reduced with increasing normal stress. This reduction is because at lower normal stresses, damage is primarily due to wear of secondary asperities. Conversely, higher normal stresses lead to more pronounced asperity interlocking and breakage of both large and small asperities, which reduces the magnitude of dilation (Karami and Stead 2007; Badt et al. 2016).

At low and medium normal stresses, both tensile- and shear-induced fractures exhibit dilation events (Figs. 2a, b, 3b, c). However, the initial occurrence of dilation events requires a greater displacement for shear-induced fractures

than for tensile-induced fractures. This is due to the formation of shear-induced fractures results in lower roughness compared to tensile fractures. Under higher normal stress conditions ($\sigma_n \geq 5$ MPa), the dilation coefficient R of shear-induced fractures decreases steadily with increasing shear displacement, and no dilation events are observed before the termination of the test (Fig. 3d, e). This also serves as evidence for the formation of low roughness shear-induced fractures under high normal stress.

4.1.3 Shear Behavior Comparison: Tensile- Versus Shear-induced Fractures

Figure 4a, b shows that tensile-induced fractures have a higher peak shear strength than shear-induced fractures for a given normal stress. There is a significant difference in both peak and ultimate shear strength between specimens with a tensile-induced fracture at all normal stresses (Fig. 4a). The significant difference between peak and ultimate shear strength at $\sigma_n = 0.5$ MPa and 3MPa indicates the low normal stress still favors shear weakening behaviors for shear-induced fractures (Fig. 4b). However, the shear-induced fractures exhibit similar peak and ultimate shear strength at $\sigma_n = 5$ MPa and 8MPa. This variable difference between peak and ultimate shear strength is attributed to differences in surface roughness.

The peak dilation angle is calculated to assess the roughness of tensile- and shear-induced fractures, as shown in Fig. 4c. It is evident that the peak dilation angle varies between 3° and 13° for both types of fractures. In addition, the peak dilation angle of the tensile-induced fracture consistently is greater than that of the shear-induced fracture for a given normal stress. This observation suggests that the tensile-induced fracture has rougher surfaces compared to the shear-induced fracture in the context of this study on red sandstone.

4.2 AE Responses of Tensile-Induced Fractures

Figure 5 shows the evolution of the AE characteristics for a tensile-induced fracture over time along with the shear stress–time curves at $\sigma_n = 1$ MPa. The AE sequence associated with the degradation of the asperities on the tensile-induced fracture shows similarities to the sequence of natural earthquakes. It manifests an accelerated rise and subsequent decay before and after the mainshock. To quantify the AE sequence, the evolution of the response rate $\dot{\Omega}$ derived from the temporal distribution of AE counts using Eq. (3) is shown in Fig. 7a, which has a similar distribution to the AE count rate shown in Fig. 5. The graph embedded in Fig. 7a indicates that the AE sequence follows a power-law relationship during the incipient shear slip (i.e., pre-peak loading stage). The exponential growth of the response

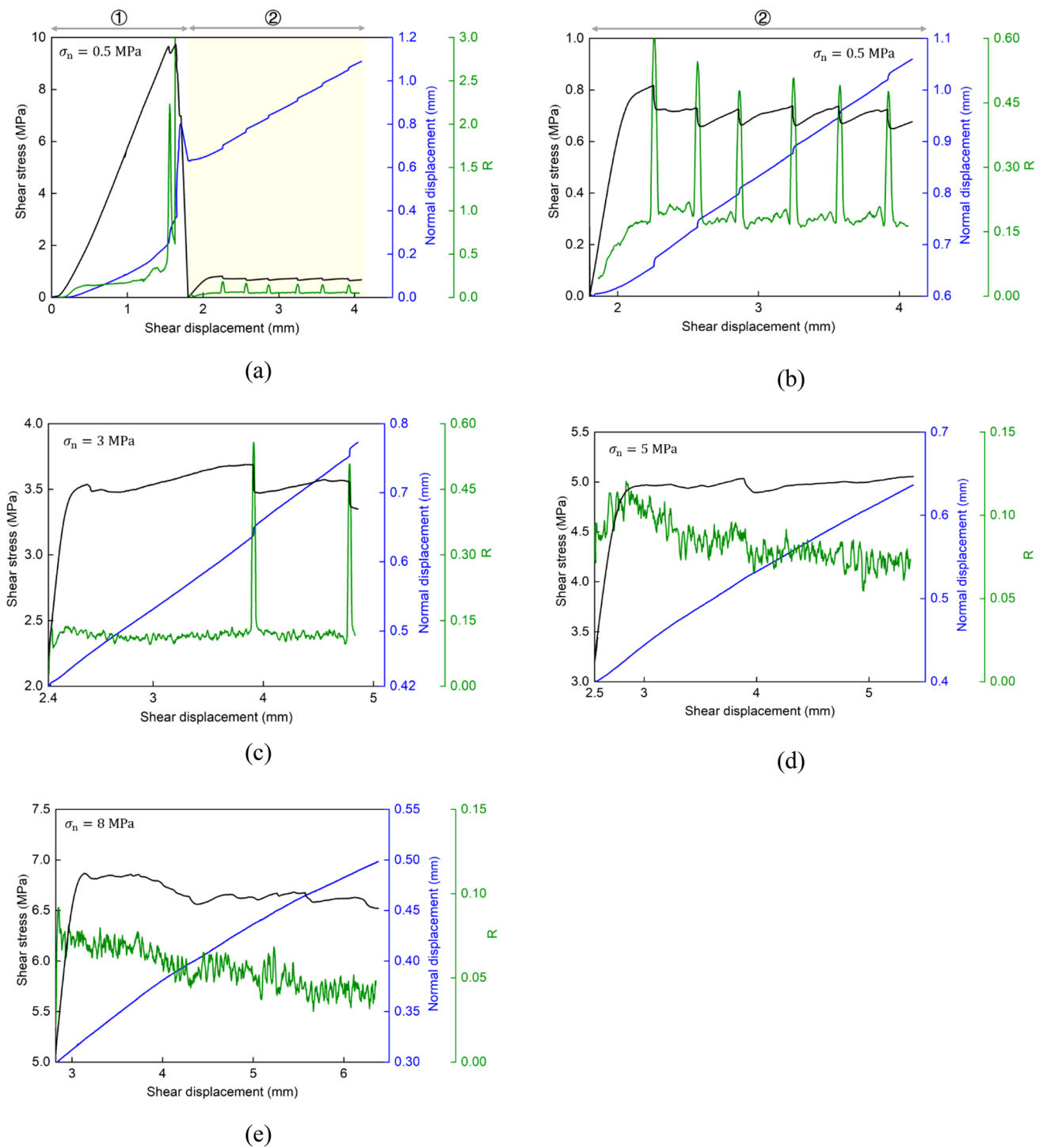


Fig. 3 Evolution of shear stress, normal displacement (δ_n), and dilation coefficient $R = d\delta_n/d\delta_s$ with shear displacement (δ_s) for specimens with a shear-induced fracture under different normal stresses. **a** Deformation evolution corresponds to the formation and shearing of the shear-induced fracture under $\sigma_n = 0.5$ MPa. Stage ① depicts the

shearing of the rock bridge, and stage ② represents the shearing of the shear-induced through-going fracture. **b** Detailed observation of stage ② in **(a)**. **c–e** Depictions of the shearing process of the shear-induced fractures under $\sigma_n = 3$ MPa, 5 MPa, and 8 MPa, respectively

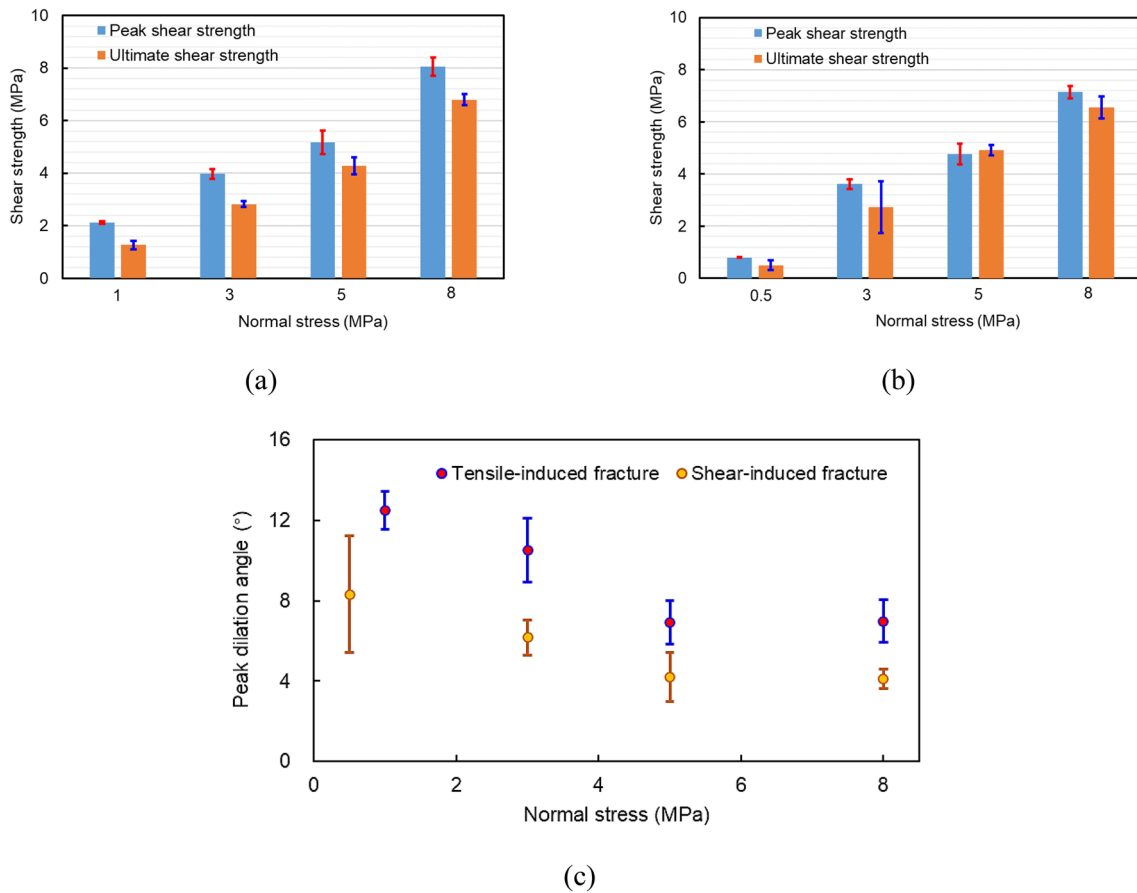


Fig. 4 Peak and ultimate shear strength for specimens with a tensile-induced fracture (a) and a shear-induced fracture (b) under different normal stresses. c Comparative analysis of the peak dilation angle between specimens with tensile- and shear-induced fractures. The peak dilation angle is determined by calculating the arctangent of

the slope of the normal-shear displacement at peak shear strength for each fracture. The histograms in (a, b) and the circles in (c) depict the average values of three specimens under identical normal stress, with error bars representing the standard deviation observed among three specimens

rate $\dot{\Omega}$ (i.e., time-interval rate) reveals the brittle fracture of a finite number of contacts that are exposed to high-stress concentrations, i.e., the Hertzian fracture mechanism (Zang et al. 2000; Lei 2003).

The post-peak response rate $\dot{\Omega}$ follows the modified Omori law (Omori 1894):

$$\dot{\Omega} = \frac{k}{(\tau + c)^p} \tag{7}$$

Here, p represents the power-law exponent ($p=1$ for the classical Omori law), while k and c are constants. Therefore, the AE sequence resulting from the shear process of the tensile-induced fracture can be described in terms of foreshocks, main shocks, and aftershocks, which is similar to the nature of earthquakes (Ouillon and Sornette 2005; Lei and Ma 2014). Based on the fitting results in Fig. 7a, the main shock occurs in the time range of $117 \text{ s} \leq \tau \leq 120 \text{ s}$, which corresponds to the period with an extremely high peak of AE

count rate and energy release, as shown in Fig. 5. The power-law singularity of the response rate $\dot{\Omega}$ at the mainshock is attributed to the fracturing of one or a few steeply inclined asperities resulting from stress concentrations.

Regarding the distribution of AE amplitudes, almost all AE events in Fig. 5 have an amplitude of less than 65 dB at $\sigma_n = 1 \text{ MPa}$. The number of events with amplitudes between 55 and 65 dB decreases significantly in the aftershock period. The AE b -value first shows a gradual decrease as the mainshock approaches and then increases during the aftershock period. Despite several stress drops in the aftershock period, there are sporadic AE events and only one notable peak in the high-energy release rate. This indicates that the stress drops are primarily due to the overriding of asperities on the tensile-formed fracture, supported by a significant increase in normal displacement and several dilation events at these stress drops, as shown in Fig. 2.

The normal stress contributes significantly to the degradation of asperities and greatly influences the energy

Fig. 5 AE responses for specimen with a tensile-induced fracture under $\sigma_n = 1$ MPa. Related AE characteristic parameters include AE count rate, b -value, amplitude, and energy release rate. The error bars represent the asymptotic error for the b -value estimation, while the smoothed curve is depicted using a sliding window of 5 consecutive data points. AE energy release in this study denotes the time integral of the square of the signal voltage at the sensor before any amplification, divided by a 10 k Ω impedance and expressed in aJ (attojoules)

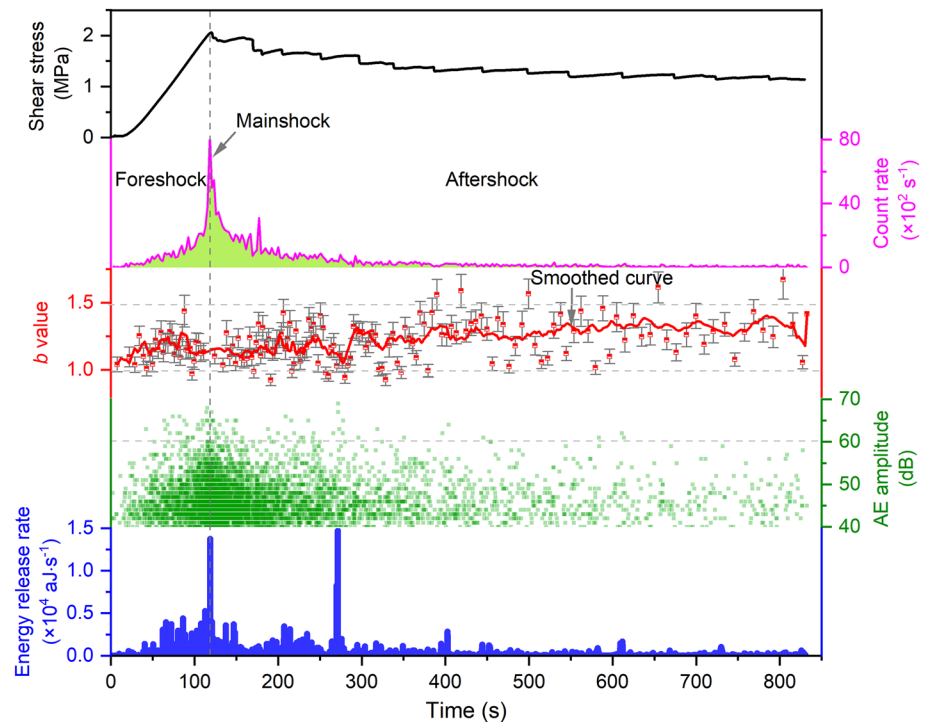
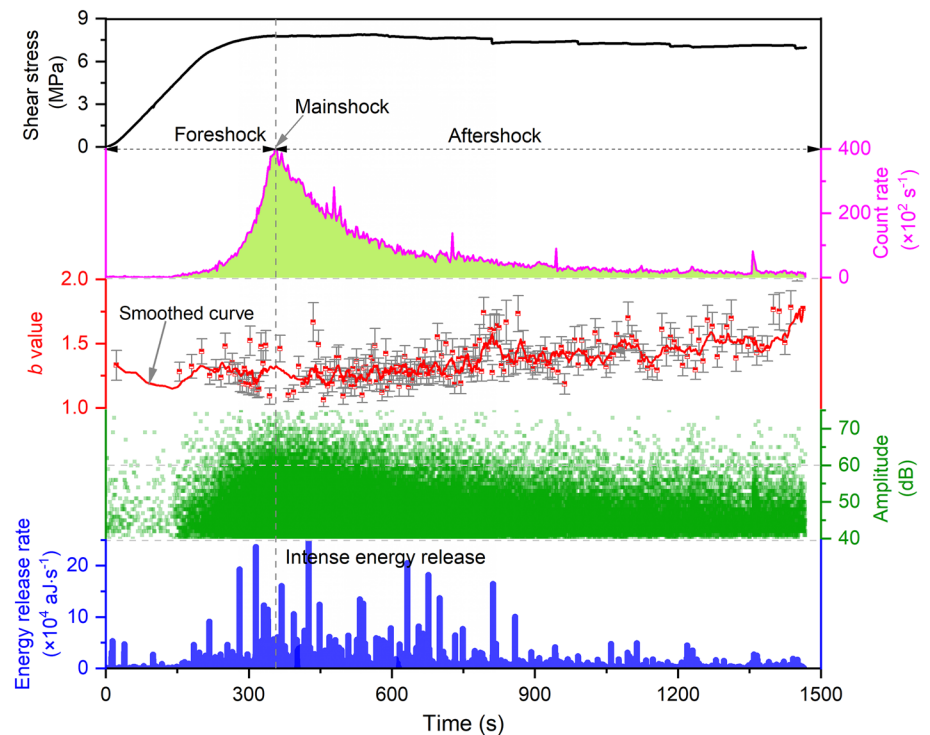


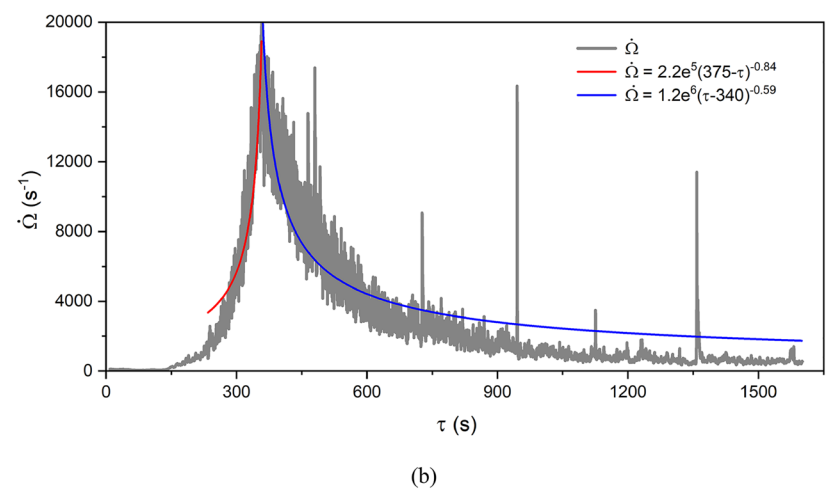
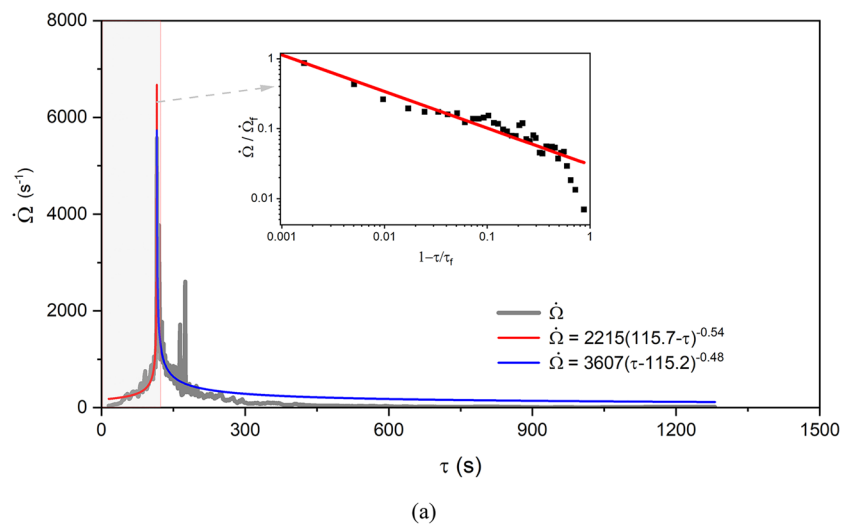
Fig. 6 The evolution of AE count rate, b -value, amplitude, and energy release rate over time during the shearing process of a tensile-induced fracture under $\sigma_n = 8$ MPa



distribution during shear slip (Badt et al. 2016). Figure 6 shows the evolution of the AE characteristics for a tensile-induced fracture under $\sigma_n = 8$ MPa. Although the shear stress does not experience a sudden drop when reaching the shear strength, the AE count rate shows a pattern of

initial growth followed by a rapid decay at the peak shear strength. As shown in Fig. 7b, both the pre- and post-peak response rates $\dot{\Omega}$ follow a power law, similar to the specimen at $\sigma_n = 1$ MPa in Fig. 7a. It is important to note that the time constants obtained by curve fitting in the two

Fig. 7 Power-law relationship of response rate $\dot{\Omega}$ with time τ for specimen with a tensile-induced fracture: **a** $\sigma_n = 1\text{MPa}$, and **b** $\sigma_n = 8\text{MPa}$. The graph embedded in **(a)** illustrates the linear fitting between the response rate $\dot{\Omega}$ and “inverse” time $(1 - \tau/\tau_f)$ in double logarithmic diagram. The gray line represents the response rate of AE counts $\dot{\Omega}$ calculated by Eq. (3). The utilized AE sequences exclusively comprise events that surpass the magnitude of completeness. The maximum $\dot{\Omega}$ corresponds to the mainshock. The distribution of the response rate before and after the mainshock obeys the power law and is fitted by Eqs. (2) and (7), depicted by the red and blue lines, respectively



power-law equations, i.e., 375 and 340, do not converge to the time at the peak response rate. This slight discrepancy may be related to the significant increase in actual contact area and the strong locking of asperities under high normal stress. The increase in contact area reduces the stress concentration at each asperity, leading to abundant energy dissipation through asperity deformation and wear during shear sliding (Grasselli 2006).

In Fig. 6, a clustered AE event is observed after $t = 140\text{ s}$, and it is noteworthy that several high-amplitude events exceeding 60 dB continue to be detected even in the aftershock period. The AE b -value initially shows a slightly decreasing trend as the mainshock approaches, similar to that observed at $\sigma_n = 1\text{ MPa}$ in Fig. 5. A progressive increase in the b -value is observed during the aftershock period, indicating an increasing proportion of small-magnitude events relative to those of larger magnitude. It is also noteworthy that the intense energy release occurs in a time domain where the shear stress is maintained close to the shear strength. As described by Badt

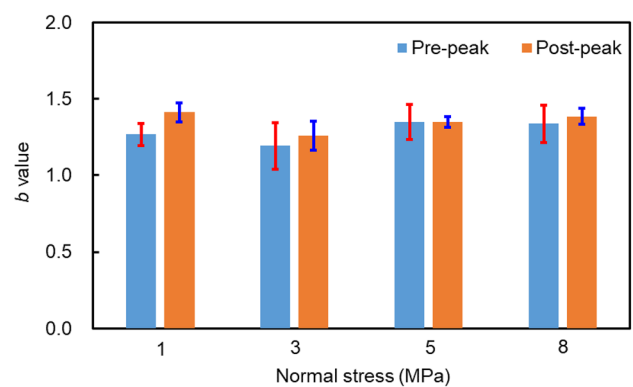


Fig. 8 Comparison of b -value for specimen with a tensile-formed fracture before and after the peak shear strength. The associated asymptotic error for the b -value estimation for all specimens is less than 0.02. The histogram illustrates the average value across three specimens with tensile-induced fracture under identical normal stress, with error bars representing the standard deviation of the b -values from these three specimens

et al. (2016), roughness enhancement occurs during the strain hardening phase, whereas gradual smoothing of the fracture surface occurs during the strain weakening phase.

Therefore, the high-stress plateau may correlate with the increase in fracture roughness under high normal stress (Boneh et al. 2014).

Fig. 9 The evolution of AE count rate, b -value, amplitude, and energy release rate over time during the shearing process of a shear-induced fracture under $\sigma_n = 0.5\text{MPa}$

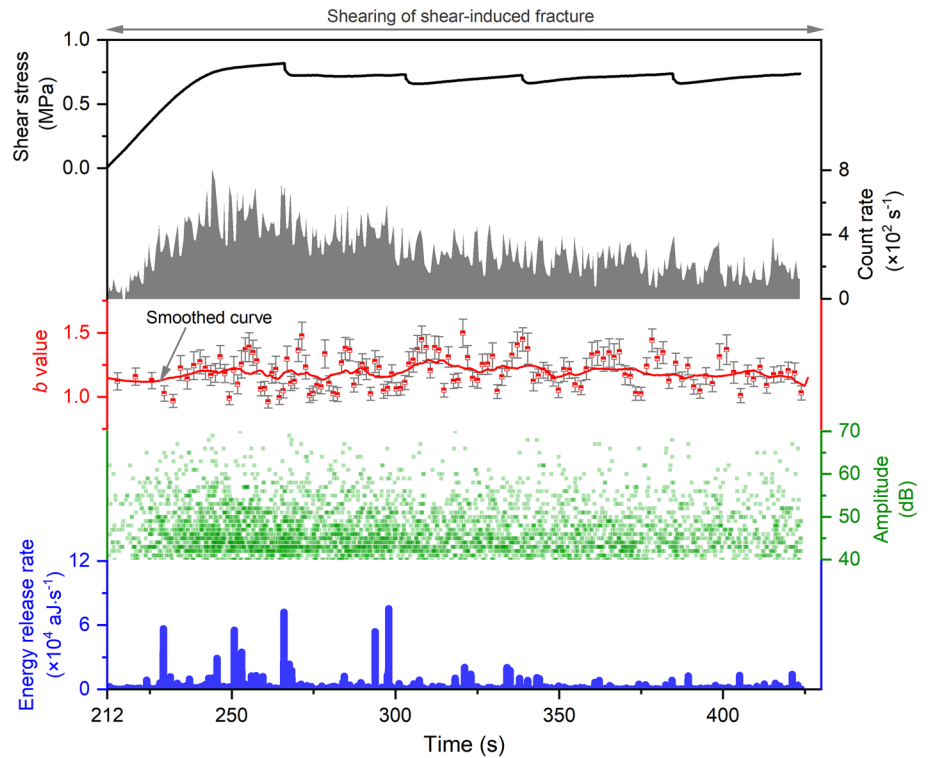


Fig. 10 The evolution of AE count rate, b -value, amplitude, and energy release rate over time during the shearing process of a shear-induced fracture under $\sigma_n = 8\text{MPa}$

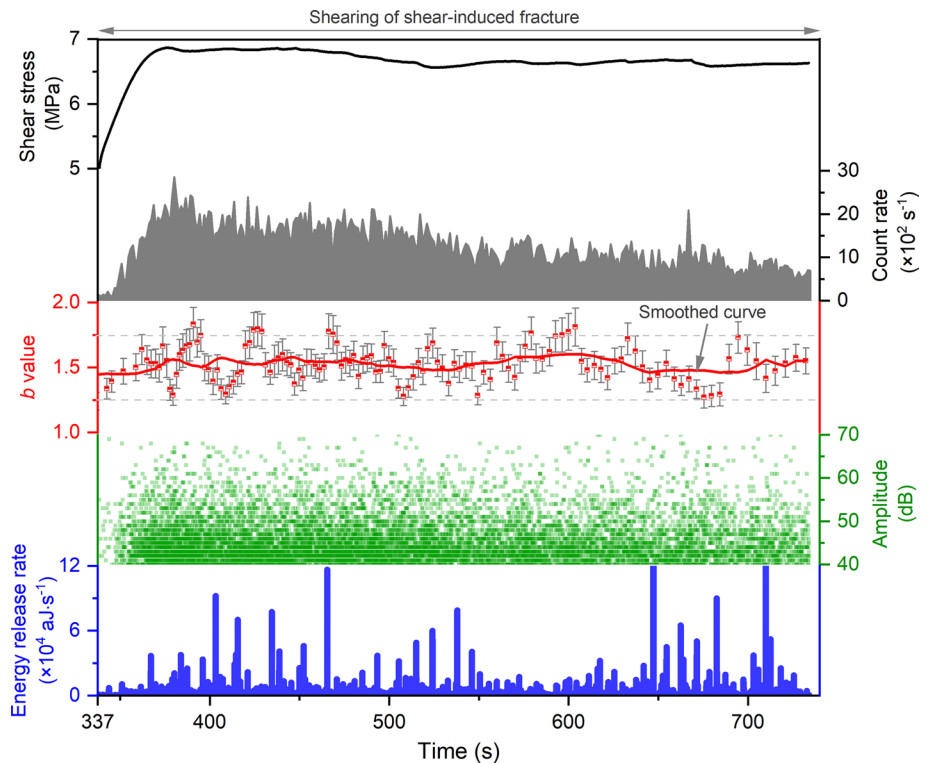


Figure 8 shows a comparison of the AE b -value for specimens with a tensile-induced fracture before and after the peak shear strength at different normal stresses. The AE b -value for tensile fractures ranges from 1.2 to 1.4 for all specimens, and the post-peak b -value is approximately equal to or slightly greater than the pre-peak b -value.

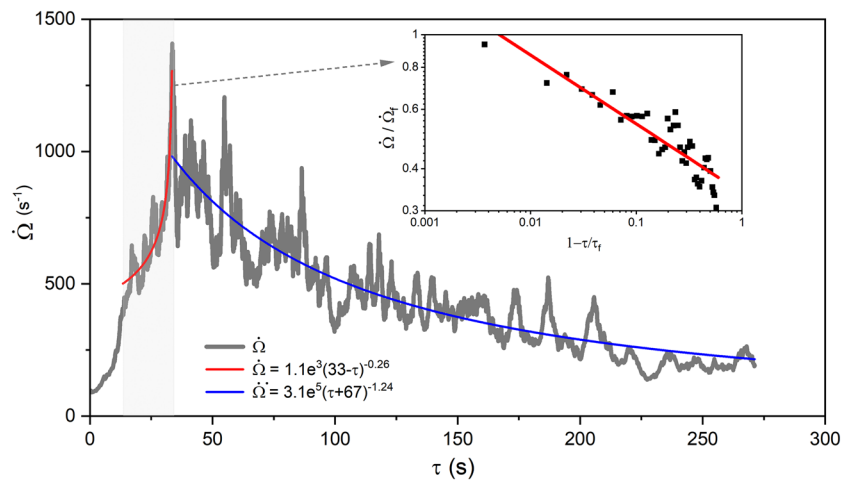
4.3 AE Responses of Shear-Induced Fractures.

Figures 9 and 10 illustrate the evolution of the AE count rate, b -value, amplitude, and energy release rate during the shear process of the shear-induced fracture at $\sigma_n = 0.5$ MPa and 8 MPa, respectively. In Fig. 9, the shear stress of the shear-induced fracture shows a remarkable nonlinear behavior near the peak shear stress, which is not obvious in the tensile-induced fracture specimens under $\sigma_n = 1$ MPa, shown in Fig. 5. The AE count rate of the shear-induced fracture increases up to the yield point and is followed by a continuous decrease, as shown in Fig. 9b. The AE b -value remains approximately constant around 1.25, indicating almost fixed ratio of low to high amplitude events. The high peaks of the energy release rate are mainly clustered before the experimental time 300 s.

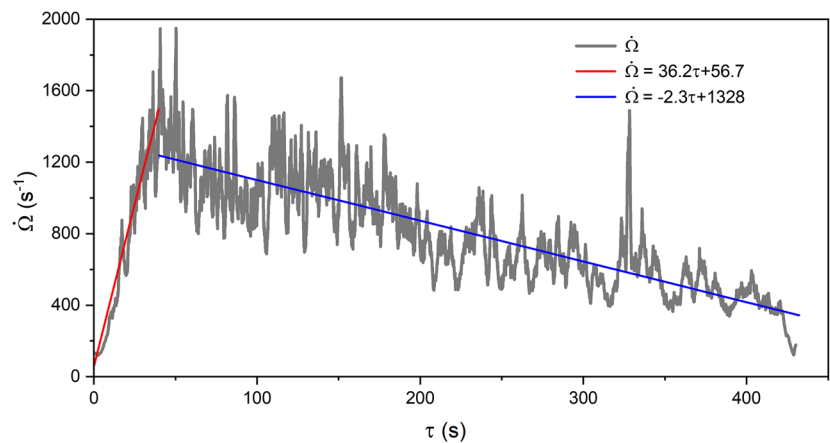
An increase in normal stress leads to a higher density of AE events, as seen in the comparison between $\sigma_n = 0.5$ MPa and 8 MPa (see Figs. 9, 10). The AE b -value in Fig. 10 remains relatively constant at 1.5, indicating a higher proportion of small-amplitude events compared to the case where $\sigma_n = 0.5$ MPa. Furthermore, the high peaks of the AE energy release rate are seen throughout the shear displacement range, in contrast to Fig. 9 where they are only seen near the peak stress at low normal stress.

Figure 11 shows the evolution of the response rate $\dot{\Omega}$ with time τ for specimen with a shear-induced fracture under $\sigma_n = 0.5$ MPa and 8MPa. The AE count rate in the shear-induced fracture shows a brief increase followed by a decay. In Fig. 11a, the response rate $\dot{\Omega}$ increases with time in a power-law relationship as it approaches the peak value, indicating an expected accelerated fracture. Although the decay time follows a power law, the fitted equation indicates the mains shock at -67 s, which is pointless. In Fig. 11b, the response rate $\dot{\Omega}$ first increases and then decays linearly at $\sigma_n = 8$ MPa, in contrast to the power-law singularity typically observed for tensile-induced fractures in Fig. 7.

Fig. 11 Evolution of response rate $\dot{\Omega}$ with time τ for specimen with a shear-induced fracture: **a** $\sigma_n = 0.5$ MPa, and **b** $\sigma_n = 8$ MPa. The graph embedded in **(a)** illustrates the linear fitting between the response rate $\dot{\Omega}$ and “inverse” time $(1 - \tau/\tau_f)$ in double logarithmic scales. The gray line represents the response rate of AE counts $\dot{\Omega}$ calculated by Eq. (3). The utilized AE sequences exclusively comprise events that surpass the magnitude of completeness. The red and blue lines represent the fitted curves for the response rate before and after reaching the maximum value



(a)



(b)

Therefore, the AE sequence from the shear process of shear-induced fractures does not resemble that observed in tensile-induced fractures, which typically include foreshocks, mainshocks, and aftershocks.

5 Discussion

5.1 Temporal Distribution of AE Response Rate

Seismic events are the manifestation of the dynamic fracturing processes occurring within the Earth's crust. The occurrence of earthquake sequences consisting of foreshocks, mainshocks, and aftershocks is typically attributed to the interplay between stresses and fault heterogeneity (Ohnaka 2003; Beeler 2004). In the laboratory, we find that tensile-induced fractures generate AE sequences similar to the hypocenter patterns observed along natural tectonic faults, i.e., foreshocks, mainshocks, and aftershocks (Fig. 7). However, in the case of shear-induced ruptures, the AE sequence does not prominently feature mainshocks and gradually diverges from the power-law function, especially as normal stress increases (Fig. 11). This divergence is thought to be due to the difference in fracture roughness and heterogeneity between tensile-induced and shear-induced fractures, factors that significantly influence seismic activity along faults both in laboratory experiments and in nature. Compared to tensile-induced fractures, the reduced roughness on the shear-induced fractures can be inferred from lower peak dilation angles (Fig. 4c). The difference in the characteristics of the fracture surfaces can also be inferred from their formation processes. The tensile fracture formed under low or suppressed confinement facilitates the development of maximum roughness correlated with grain size. On the other hand, the compressive-shear stress generally leads to grain and asperity shearing, resulting in lower roughness of the shear-induced fracture. The presence of debris and gouge material on the shear-induced fractures is also indicative of the shear history during their formation. Goebel et al. (2013a) observed that aftershock sequences were constrained to faults that evolved from fracture surfaces with significant heterogeneity, whereas they were absent from saw-cut surfaces in their experiments. This highlights the importance of fault heterogeneity in the temporal clustering of seismic sequences.

Foreshocks are typically correlated with the rupture of immobilized patches, which increases the stress in the surrounding areas and promotes the cascade triggering both the subsequent foreshock events and the eventual mainshock (Liu et al. 2022; Bolton et al. 2023; Gu et al. 2023). Therefore, the power acceleration of the AE sequence is a manifestation of cascade triggering and the gradual "unpinning" of the fault. Fault heterogeneity is considered to be

the dominant control factor for the cascade triggering of both foreshocks and mainshocks (Cattania and Segall 2021; Liu et al. 2022). Thus, we can attribute the difference in the temporal distribution of the AE sequence to the difference in the heterogeneity between tensile and shear-induced ruptures. The absence of acceleration before the mainshock suggests that the structure on shear-induced fractures is not conducive to energy accumulation and cascade triggering does not occur (Fig. 11).

The hypothesis of aftershocks suggests that their occurrence depends on a secondary redistribution of stress following the mainshock (Beeler 2004; Freed 2005). Observations of both natural and laboratory earthquakes indicate that aftershocks predominantly occur outside or near the margins of the source areas (Mendoza and Hartzell 1988; Lei 2003). Therefore, the power-law decay following the Omori law in tensile-induced fractures is a consequence of stress redistribution among the patches around the mainshock area, and a strong interaction between AE events is exhibited (Fig. 7). The absence of the mainshock and a power-law aftershock sequence in shear-induced fractures in our experiments suggests that there is no causal relationship between AE events during the shear of the shear-induced fracture (Fig. 11).

5.2 Temporal Evolution of AE b -value

The AE b -value characterizes the correlation between the number of earthquakes and their magnitude and serves as a descriptor of the stress and fracture state of a rock volume. Load-bearing asperities have the potential to generate clusters of relatively larger-magnitude events due to local stress increases, resulting in the formation of low b -value regions (Lei 2003; Goebel et al. 2013b; Geffers et al. 2022). Because clusters of low b -values represent stress concentrations in specific patches, anomalous b -values have been used to characterize fault heterogeneity (Lei 2003; Goebel et al. 2012).

The AE b -value of the tensile fracture undergoes a decrease before the foreshock, which is attributed to the failure of individual asperities due to stress concentration (Figs. 5, 6). This corresponds to the sharp increase in the AE count rate and high amplitude events. As pointed out by Lei et al. (2004), a long-term decreasing trend and short-term fluctuation of the b -value before dynamic rupture can be considered as characteristics of heterogeneous fault failure. In addition, the gradual increase of the AE b -value also indicates the decrease of the local stress concentration, indicating an increasing proportion of small-amplitude events (Figs. 5, 6). The nearly constant b -value throughout the shear process of shear-induced fractures indicates the absence of significant stress heterogeneity across the fracture surface (Figs. 9, 10).

As a result, analysis of the earthquake magnitude distributions can help to estimate the state of the fault. Variable

AE b -values characterize faults with pronounced roughness and heterogeneity, typically found in young tectonic faults or fractures. Conversely, nearly unchanged b -values may indicate shear sliding along well-developed, small, mature faults that tend to be homogeneous. It is worth noting that the fractures in this study represent an end member, and the nature of fractures or faults is more complex. As pointed out by Einstein (2021), what may appear to be tensile or shear fractures on a large scale are produced by a combination of tensile and shear mechanisms on a smaller scale.

5.3 Implication

Fault heterogeneity is considered the primary factor contributing to natural earthquakes, resulting in seismic patterns from tectonic faults (Morad et al. 2022; Goebel et al. 2023). These patterns often include foreshocks, mainshocks, and aftershocks. Tensile-induced fractures, characterized by high roughness and heterogeneity, can be used to reproduce the fault with significant heterogeneity in the laboratory. The heterogeneous fractures or faults exhibit seismicity precursors characterized by a power-law distribution and decreasing b -values during shear process. These precursor indicators can be used to potentially identify and mitigate the risks associated with the induced earthquakes during the deployment of energy extraction technologies, including enhanced geothermal systems, unconventional hydrocarbons such as shale gas, and wastewater injection (Hofmann et al. 2019; Kolawole et al. 2019). In contrast, shear-induced fractures with lower roughness can be used to replicate more homogeneous faults characterized by lower roughness. Experimental results suggest that identifying the rupture of the homogeneous fault is challenging.

6 Conclusions

Direct shear tests were performed on tensile- and shear-induced fractures using the AE technique to monitor rock cracking. The primary objective was to clarify the similarities and differences in shear characteristics and microcracking behavior between tensile- and shear-induced fractures. The main results are summarized below:

- (1) Shear-induced fractures exhibit lower peak shear strength and dilation angle than tensile-induced fractures for a given normal stress. As normal stress increases, the frequency of normal dilation events decreases and the interval time between two adjacent dilation events increases for both tensile-induced and shear-induced fractures. Dilation events are more likely to occur in tensile-induced fractures than in
- (2) Tensile-induced fractures exhibit AE sequences similar to seismic patterns observed in natural earthquakes, with foreshocks, mainshocks, and aftershocks. The power-law distribution of AE sequences before and after the mainshock is indicative of cascade triggering and stress redistribution between asperities, respectively. This suggests high roughness and heterogeneity on the tensile-induced fractures. In contrast, the AE sequence for shear-induced fractures lacks prominent mainshocks and deviates progressively from the power-law function with increasing normal stress, indicating a relatively homogeneous structure on the shear-induced fractures.
- (3) The AE b -value first shows a gradual decrease as the mainshock approaches and then slowly increases during the aftershock period for tensile-induced fractures. In contrast, the b -value for shear-induced fractures remains almost constant throughout the shear process. The difference between tensile- and shear-induced fractures indicates that the evolution of the b -value can help to identify whether the fault is highly heterogeneous.

Acknowledgements We appreciate the comments of our anonymous reviewers to improve the quality of our manuscript.

Funding This work was supported by the National Natural Science Foundation of China (Grant No. 52125903). The first author expresses gratitude to the Alexander von Humboldt Foundation for providing financial support for her postdoctoral research at the Helmholtz Centre Potsdam GFZ German Research Centre for Geosciences. HH and YJ kindly acknowledge the financial support of the Helmholtz Association's Initiative and Networking Fund for the Helmholtz Young Investigator Group ARES (Contract Number VH-NG-1516).

Data Availability Data will be made available on request.

Declarations

Conflict of interest The authors declare that they have no known competing financial interests or personal relationships that could have appeared to influence the work reported in this paper.

References

- Amorèse D (2007) Applying a change-point detection method on frequency-magnitude distributions. *Bull Seismol Soc Am* 97(5):1742–1749
- Badt N, Hatzor YH, Toussaint R, Sagy A (2016) Geometrical evolution of interlocked rough slip surfaces: the role of normal stress. *Earth Planet Sci Lett* 443:153–161
- Beeler NM (2004) Review of the physical basis of laboratory-derived relations for brittle failure and their implications for earthquake occurrence and earthquake nucleation. *Pure Appl Geophys*. <https://doi.org/10.1007/s00024-004-2536-z>

- Bolton DC, Shreedharan S, Riviere J, Marone C (2021) Frequency-magnitude statistics of laboratory foreshocks vary with shear velocity, fault slip rate, and shear stress. *J Geophys Res Solid Earth* 126(11):e2021JB022175
- Bolton DC, Marone C, Saffer D, Trugman DT (2023) Foreshock properties illuminate nucleation processes of slow and fast laboratory earthquakes. *Nat Commun* 14(1):3859
- Boneh Y, Chang JC, Lockner DA, Reches Z (2014) Evolution of wear and friction along experimental faults. *Pure Appl Geophys* 171(11):3125–3141
- Borate P, Riviere J, Marone C, Mali A, Kifer D, Shokouhi P (2023) Using a physics-informed neural network and fault zone acoustic monitoring to predict lab earthquakes. *Nat Commun* 14(1):3693
- Byerlee JD (1970) The mechanics of stick-slip. *Tectonophysics* 9(5):475–486
- Cattania C, Segall P (2021) Precursory Slow Slip and foreshocks on rough faults. *J Geophys Res: Solid Earth*. <https://doi.org/10.1029/2020JB020430>
- Chen B-R, Feng X-T, Li Q-P, Luo R-Z, Li S (2013) Rock burst intensity classification based on the radiated energy with damage intensity at Jinping II hydropower station, China. *Rock Mech Rock Eng* 48(1):289–303
- Cui G, Zhang C, Ye J, Zhou H, Li L, Zhang L (2022) Influences of dynamic normal disturbance and initial shear stress on fault activation characteristics. *Geomech Geophys Geo-Energy Georour*. <https://doi.org/10.1007/s40948-022-00463-6>
- Davidesko G, Sagy A, Hatzor YH (2014) Evolution of slip surface roughness through shear. *Geophys Res Lett* 41(5):1492–1498
- Daividsen J, Stanchits S, Dresen G (2007) Scaling and universality in rock fracture. *Phys Rev Lett* 98(12):125502
- Dresen G, Kwiatek G, Goebel T, Ben-Zion Y (2020) Seismic and aseismic preparatory processes before large stick-slip failure. *Pure Appl Geophys* 177(12):5741–5760
- Einstein HH (2021) Fractures: tension and shear. *Rock Mech Rock Eng* 54(7):3389–3408
- Freed AM (2005) Earthquake triggering by static, dynamic, and post-seismic stress transfer. *Annu Rev Earth Planet Sci* 33(1):335–367
- Geffers GM, Main IG, Naylor M (2022) Biases in estimating b-values from small earthquake catalogues: how high are high b-values? *Geophys J Int* 229(3):1840–1855
- Goebel THW, Becker TW, Schorlemmer D, Stanchits S, Sammis C, Rybacki E, Dresen G (2012) Identifying fault heterogeneity through mapping spatial anomalies in acoustic emission statistics. *J Geophys Res Solid Earth*. <https://doi.org/10.1029/2011JB008763>
- Goebel THW, Sammis CG, Becker TW, Dresen G, Schorlemmer D (2013a) A comparison of seismicity characteristics and fault structure between stick-slip experiments and nature. *Pure Appl Geophys* 172(8):2247–2264
- Goebel THW, Schorlemmer D, Becker TW, Dresen G, Sammis CG (2013b) Acoustic emissions document stress changes over many seismic cycles in stick-slip experiments. *Geophys Res Lett* 40(10):2049–2054
- Goebel THW, Brodsky EE, Dresen G (2023) Fault roughness promotes earthquake-like aftershock clustering in the lab. *Geophys Res Lett*. <https://doi.org/10.1029/2022GL101241>
- Grasselli G (2006) Manuel rocha medal recipient shear strength of rock joints based on quantified surface description. *Rock Mech Rock Eng* 39(4):295–314
- Gu L, Hao S, Elsworth D (2023) Precursory predictors of the onset of stick-slip frictional instability. *Int J Solids Struct* 264:112119
- Gutenberg B, Richter CF (1944) Frequency of earthquakes in California. *Bull Seismol Soc Am* 34:185–188
- Hao S-W, Rong F, Ming-Fu L, Wang H-Y, Xia M-F, Fu-Jiu K, Bai Y-L (2013) Power-law singularity as a possible catastrophe warning observed in rock experiments. *Int J Rock Mech Min Sci* 60:253–262
- Hardebeck JL, Felzer KR, Michael AJ (2008) Improved tests reveal that the accelerating moment release hypothesis is statistically insignificant. *J Geophys Res Solid Earth*. <https://doi.org/10.1029/2007JB005410>
- Hofmann H et al (2019) First field application of cyclic soft stimulation at the Pohang Enhanced Geothermal System site in Korea. *Geophys J Int* 217(2):926–949
- Ji Y, Hofmann H, Duan K, Zang A (2022a) Laboratory experiments on fault behavior towards better understanding of injection-induced seismicity in geoelectric systems. *Earth Sci Rev* 226:103910
- Ji Y, Wang L, Hofmann H, Kwiatek G, Dresen G (2022b) High-rate fluid injection reduces the nucleation length of laboratory earthquakes on critically stressed faults in granite. *Geophys Res Lett*. <https://doi.org/10.1029/2022GL100418>
- Jiang Q, Yang B, Yan F, Liu C, Shi Y, Li L (2020) New method for characterizing the shear damage of natural rock joint based on 3D engraving and 3D scanning. *Int J Geomech*. [https://doi.org/10.1061/\(ASCE\)GM.1943-5622.0001575](https://doi.org/10.1061/(ASCE)GM.1943-5622.0001575)
- Johansson F (2016) Influence of scale and matedness on the peak shear strength of fresh, unweathered rock joints. *Int J Rock Mech Min Sci* 82:36–47
- Karami A, Stead D (2007) Asperity degradation and damage in the direct shear test: a hybrid FEM/DEM approach. *Rock Mech Rock Eng* 41(2):229–266
- Kim Y-S, Peacock DCP, Sanderson DJ (2003) Mesoscale strike-slip faults and damage zones at Marsalforn, Gozo Island, Malta. *J Struct Geol* 25(5):793–812
- Kolawole F et al (2019) The susceptibility of Oklahoma's basement to seismic reactivation. *Nat Geosci* 12(10):839–844
- Lei X (2003) How do asperities fracture? An experimental study of unbroken asperities. *Earth Planet Sci Lett* 213(3–4):347–359
- Lei X, Ma S (2014) Laboratory acoustic emission study for earthquake generation process. *Earthq Sci* 27(6):627–646
- Lei X et al (2004) Detailed analysis of acoustic emission activity during catastrophic fracture of faults in rock. *J Struct Geol* 26(2):247–258
- Li B, Jiang Y, Mizokami T, Ikusada K, Mitani Y (2014) Anisotropic shear behavior of closely jointed rock masses. *Int J Rock Mech Min Sci* 71:258–271
- Li Y, Du X, Ji Y (2022) Prediction of the transitional normal stress of rock joints under shear. *Int J Rock Mech Min Sci* 159:105203
- Liu X, Xu W, He Z, Fang L, Chen Z (2022) Aseismic slip and cascade triggering process of foreshocks leading to the 2021 Mw 6.1 Yangbi earthquake. *Seismol Res Lett* 93(3):1413–1428
- Luo G, Qi S, Zheng B (2022) Rate effect on the direct shear behavior of granite rock bridges at low to subseismic shear rates. *J Geophys Res Solid Earth*. <https://doi.org/10.1029/2022JB024348>
- Marty S et al (2023) Nucleation of laboratory earthquakes: quantitative analysis and scalings. *J Geophys Res Solid Earth*. <https://doi.org/10.1029/2022JB026294>
- Mendoza C, Hartzell SH (1988) Aftershock patterns and main shock faulting. *Bull Seismol Soc Am* 78(4):1438–1449
- Meng F, Zhou H, Li S, Zhang C, Wang Z, Kong L, Zhang L (2016a) Shear behaviour and acoustic emission characteristics of different joints under various stress levels. *Rock Mech Rock Eng* 49(12):4919–4928
- Meng F, Zhou H, Wang Z, Zhang L, Kong L, Li S, Zhang C (2016b) Experimental study on the prediction of rockburst hazards induced by dynamic structural plane shearing in deeply buried hard rock tunnels. *Int J Rock Mech Min Sci* 86:210–223
- Meng F, Wong LNY, Guo T (2022) Frictional behavior and micro-damage characteristics of rough granite fractures. *Tectonophysics* 842:229589

- Miao ST, Pan PZ, Zhang CQ, Huo L (2024) Shear band evolution and acoustic emission characteristics of sandstone containing non-persistent flaws. *J Rock Mech Geotech Eng* 16(2):497–513. <https://doi.org/10.1016/j.jrmge.2023.04.003>
- Morad D, Sagy A, Hatzor YH (2020) The significance of displacement control mode in direct shear tests of rock joints. *Int J Rock Mech Min Sci* 134:104444
- Morad D, Sagy A, Tal Y, Hatzor YH (2022) Fault roughness controls sliding instability. *Earth Planet Sci Lett* 579:117365
- Morgan SP, Johnson CA, Einstein HH (2013) Cracking processes in Barre granite: fracture process zones and crack coalescence. *Int J Fract* 180(2):177–204
- Myers R, Aydin A (2004) The evolution of faults formed by shearing across joint zones in sandstone. *J Struct Geol* 26(5):947–966
- Niktabar SMM, Rao KS, Shrivastava AK (2017) Effect of rock joint roughness on its cyclic shear behavior. *J Rock Mech Geotech Eng* 9(6):1071–1084
- Ohnaka M (2003) A constitutive scaling law and a unified comprehension for frictional slip failure, shear fracture of intact rock, and earthquake rupture. *J Geophys Res Solid Earth*. <https://doi.org/10.1029/2000JB000012>
- Omori F (1894) On the after-shocks of earthquakes. *J Coll Sci Imp Univ Tokyo* 7:111–120
- Ouillon G, Sornette D (2005) Magnitude-dependent Omori law: theory and empirical study. *J Geophys Res Solid Earth* 110:4. <https://doi.org/10.1029/2004JB003311>
- Sagy A, Brodsky EE, Axen GJ (2007) Evolution of fault-surface roughness with slip. *Geology* 35(3):283
- Singh HK, Basu A (2016) Shear behaviors of 'real' natural un-matching joints of granite with equivalent joint roughness coefficients. *Eng Geol* 211:120–134
- Tang ZC, Wong LNY (2015) New criterion for evaluating the peak shear strength of rock joints under different contact states. *Rock Mech Rock Eng* 49(4):1191–1199
- Triantis D, Kourkoulis SK (2018) An alternative approach for representing the data provided by the acoustic emission technique. *Rock Mech Rock Eng* 51(8):2433–2438
- Vogler D, Walsh SDC, Bayer P, Amann F (2017) Comparison of surface properties in natural and artificially generated fractures in a crystalline rock. *Rock Mech Rock Eng* 50(11):2891–2909
- Voight B (1988) A method for prediction of volcanic eruptions. *Nature* 332(6160):125–130
- Vulcanologia INDGE, Bologna S, Bologna I (2003) A review and new insights on the estimation of the b-value and its uncertainty. *Ann Geophys* 46:1271–1282
- Yang ZY, Di CC, Yen KC (2001) The effect of asperity order on the roughness of rock joints. *Int J Rock Mech Min Sci* 38(5):745–752
- Zang A, Wagner FC, Stanchits S, Janssen C, Dresen G (2000) Fracture process zone in granite. *J Geophys Res: Solid Earth* 105(B10):23651–23661
- Zhang JZ, Zhou XP (2020) Forecasting Catastrophic Rupture in Brittle Rocks Using Precursory AE Time Series. *J Geophys Res Solid Earth*. <https://doi.org/10.1029/2019JB019276>
- Zhang C, Cui G, Deng L, Zhou H, Lu J, Dai F (2019) Laboratory investigation on shear behaviors of bolt–grout interface subjected to constant normal stiffness. *Rock Mech Rock Eng* 53(3):1333–1347
- Zhang C, Xu J, Jin S, Cui G, Guo Y, Li L (2022) Sliding modes of fault activation under constant normal stiffness conditions. *J Rock Mech Geotech Eng* 15:1213–1225
- Zhang X-P, Sun W, Zhang Q, Xie X (2023) Can the splitting joint reproduce the characteristics of the natural joint in the lab?—A comparison study based on the roughness analysis and shear test. *Eng Geol* 324:107246

Publisher's Note Springer Nature remains neutral with regard to jurisdictional claims in published maps and institutional affiliations.

Springer Nature or its licensor (e.g. a society or other partner) holds exclusive rights to this article under a publishing agreement with the author(s) or other rightsholder(s); author self-archiving of the accepted manuscript version of this article is solely governed by the terms of such publishing agreement and applicable law.